
Many-body Approximation for Non-negative Tensors

Kazu Ghalamkari

RIKEN AIP

kazu.ghalamkari@riken.jp

Mahito Sugiyama

National Institute of Informatics
SOKENDAI
mahito@nii.ac.jp

Yoshinobu Kawahara

Osaka University
RIKEN AIP
kawahara@ist.osaka-u.ac.jp

Abstract

We present an alternative approach to decompose non-negative tensors, called *many-body approximation*. Traditional decomposition methods assume low-rankness in the representation, resulting in difficulties in global optimization and target rank selection. We avoid these problems by energy-based modeling of tensors, where a tensor and its mode correspond to a probability distribution and a random variable, respectively. Our model can be globally optimized in terms of the KL divergence minimization by taking the *interaction between variables*, *i.e.* *modes*, into account that can be tuned more intuitively than ranks. Furthermore, we visualize interactions between modes as *tensor networks* and reveal a nontrivial relationship between many-body approximation and low-rank approximation. We demonstrate the effectiveness of our approach in tensor completion and approximation.

1 Introduction

Tensors are generalization of vectors and matrices. Data in various fields such as neuroscience [8], bioinformatics [22], signal processing [7], and computer vision [32] are often stored in the form of tensors, and features are extracted from them. *Tensor decomposition* and its non-negative version [35] are popular methods to extract features by approximating tensors by the sum of products of smaller tensors. It usually tries to minimize the reconstruction error, the difference between an original tensor and the tensor reconstructed from obtained smaller tensors.

In tensor decomposition approaches, a *low-rank structure* is typically assumed, where a given tensor is essentially represented by a linear combination of a small number of bases. Such decomposition requires the following two kinds of information. First, it requires the structure, which specifies the type of decomposition such as CP decomposition [13] and Tucker decomposition [40]. More recently, *tensor networks* [6] have been introduced, which can intuitively and flexibly design the structure including tensor train decomposition [31], tensor ring decomposition [46], and tensor tree decomposition [26]. Second, it requires the number of bases used in the decomposition, often referred to as the rank. Larger ranks increase the capability of the model while increasing the computational cost, hence the user needs to find the appropriate rank in this tradeoff problem. Since these low-rank structure based decomposition via reconstruction error minimization is non-convex, which causes initial value dependence [15, Chapter 3], the problem of finding an appropriate setting of the low-rank structure is highly nontrivial in practice as it is hard to locate the cause if the decomposition does not perform well. As a result, to find proper structure and rank, the user often needs to perform decomposition multiple times with various settings, which is time and memory consuming.

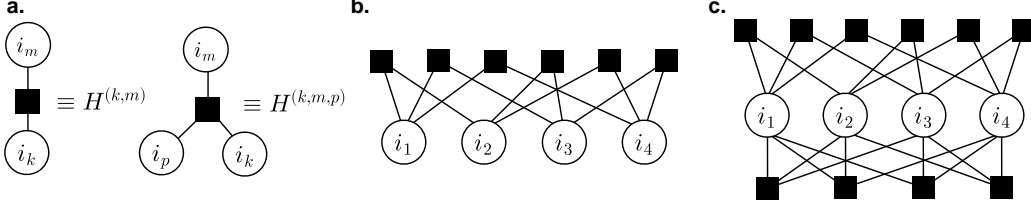


Figure 1: Interaction representations corresponding to (a) second and third order energy (b) two- and (c) three-body approximation.

Instead of the low-rank structure that has been the focus of attention in the past, in this paper, we propose a novel formulation of non-negative tensor decomposition, called *many-body approximation*, that focuses on the relationship among modes of tensors. The structure of decomposition can be naturally determined based on the existence of the interactions between modes. The proposed method requires only the decomposition structure and does not require the rank value, which traditional decomposition methods also require as a hyperparameter and often suffer to determine.

To describe interactions between modes, we follow the standard strategy in statistical mechanics that uses an energy function $\mathcal{H}(\cdot)$ to treat interactions and considers the corresponding distribution $\exp(-\mathcal{H}(\cdot))$. This model is known to be an energy-based model in machine learning [18] and is exploited in tensor decomposition as Legendre decomposition [39]. Technically, it parameterizes a tensor as a discrete probability distribution and reduces the number of parameters by enforcing some of them to be zero in optimization. We explore this energy-based approach further and discover the family of parameter sets that represent interactions between modes in the energy function $\mathcal{H}(\cdot)$. How to choose non-zero parameters in Legendre decomposition has been an open problem, and we firstly address this problem and propose many-body approximation as a special case of Legendre decomposition. Moreover, although Legendre decomposition is not factorization of tensors in general, our proposal always offers factorization, which can reveal patterns in tensors. Since the advantage of Legendre decomposition is inherited to our proposal, many-body approximation can be achieved by convex optimization that globally minimizes the Kullback–Leibler (KL) divergence [17].

Furthermore, we introduce a way of representing mode interactions, which visualizes the presence or absence of interactions between modes as a diagram. We discuss the relation to the tensor network and point out that an operation called coarse-grained transformation [20], in which multiple tensors are viewed as a new tensor, reveals unexpected relationship between the proposed method and existing methods such as tensor ring and tensor tree decomposition.

We summarize our contribution as follows:

- By focusing on the interaction between modes of tensors, we introduce rank-free tensor decomposition, called many-body approximation. This decomposition is achieved by convex optimization.
- We present a way of describing tensor many-body approximation, interaction representation, a diagram that shows interactions within a tensor and can be transformed into tensor networks.
- Many-body approximation can perform tensor completion via the *em*-algorithm, which empirically shows better performance than low-rank based existing methods.

2 Many-body Approximation for Tensors

Our proposal, many-body approximation, is based on the formulation of Legendre decomposition for tensors, which we first review in Section 2.1. Then we introduce interactions between modes and its visual representation in Section 2.2, many-body approximation in Section 2.3, and transformation of interaction representation into tensor networks in Section 2.4. In the following discussion, we consider D -order non-negative tensors with the size (I_1, \dots, I_D) , and we denote by $[K] = \{1, 2, \dots, K\}$ for a positive integer K . We assume the sum of all elements in a given tensor to be 1 for simplicity, while this assumption can be eliminated using the general property of the Kullback–Leibler (KL) divergence, $\lambda D_{KL}(\mathcal{P}, \mathcal{Q}) = D_{KL}(\lambda \mathcal{P}, \lambda \mathcal{Q})$, for any $\lambda \in \mathbb{R}_{>0}$.

2.1 Reminder to Legendre Decomposition and its optimization

Legendre decomposition is a method to decompose a non-negative tensor by regarding the tensor as a discrete distribution and representing it with a limited number of parameters. We describe a non-negative tensor \mathcal{P} using parameters $\boldsymbol{\theta} = (\theta_{2,\dots,1}, \dots, \theta_{I_1,\dots,I_D})$ and its energy function \mathcal{H} as

$$\mathcal{P}_{i_1,\dots,i_D} = \exp(-\mathcal{H}_{i_1,\dots,i_D}), \quad \mathcal{H}_{i_1,\dots,i_D} = -\sum_{i'_1=1}^{i_1} \dots \sum_{i'_D=1}^{i_D} \theta_{i'_1,\dots,i'_D}, \quad (1)$$

where $\theta_{1,\dots,1}$ has a role of normalization. It is clear that the index set of a tensor corresponds to sample space of a distribution and the value of each entry of the tensor is regarded as the probability of realizing the corresponding index [38].

As we see in Equation (1), we can uniquely identify tensors from the parameters $\boldsymbol{\theta}$. Inversely, we can compute $\boldsymbol{\theta}$ from a given tensor as

$$\theta_{i_1,\dots,i_D} = \sum_{i'_1=1}^{I_1} \dots \sum_{i'_D=1}^{I_D} \mu_{i_1,\dots,i_D}^{i'_1,\dots,i'_D} \log \mathcal{P}_{i'_1,\dots,i'_D} \quad (2)$$

using the Möbius function $\mu : S \times S \rightarrow \{-1, 0, +1\}$, where S is the set of indices, defined inductively as follows:

$$\mu_{i_1,\dots,i_D}^{i'_1,\dots,i'_D} = \begin{cases} 1 & \text{if } i_d = i'_d, \forall d \in [D], \\ -\prod_{d=1}^D \sum_{j_d=i_d}^{i'_d-1} \mu_{i_1,\dots,i_D}^{j_1,\dots,j_D} & \text{else if } i_d \leq i'_d, \forall d \in [D], \\ 0 & \text{otherwise.} \end{cases}$$

Since distribution described by Equation (1) belongs to the exponential family, $\boldsymbol{\theta}$ corresponds to natural parameters of the exponential family, and we can also identify each tensor by expectation parameters $\boldsymbol{\eta} = (\eta_{2,\dots,1}, \dots, \eta_{I_1,\dots,I_D})$ using Möbius inversion as

$$\eta_{i_1,\dots,i_D} = \sum_{i'_1=i_1}^{I_1} \dots \sum_{i'_D=i_D}^{I_D} \mathcal{P}_{i'_1,\dots,i'_D}, \quad \mathcal{P}_{i_1,\dots,i_D} = \sum_{i'_1=1}^{I_1} \dots \sum_{i'_D=1}^{I_D} \mu_{i_1,\dots,i_D}^{i'_1,\dots,i'_D} \eta_{i'_1,\dots,i'_D}, \quad (3)$$

where $\eta_{1,\dots,1} = 1$ because of normalization. See Section A in Supplement for examples of the above calculation. Since distribution is determined by specifying either θ -parameters or η -parameters, they form two coordinate systems called the θ -coordinate system and the η -coordinate system, respectively.

2.1.1 Optimization

Legendre decomposition approximates a tensor by setting some θ values to be zero, which corresponds to dropping some parameters for regularization. It achieves convex optimization using the dual flatness of θ - and η -coordinate systems. Let B be the set of indices of θ parameters that are not imposed to be 0. Then Legendre decomposition coincides with a projection of a given nonnegative tensor \mathcal{P} onto the subspace $\mathcal{B} = \{\mathcal{Q} \mid \theta_{i_1,\dots,i_D} = 0 \text{ if } (i_1, \dots, i_D) \notin B \text{ for } \theta\text{-parameters of } \mathcal{Q}\}$.

Let us consider projection of a given tensor \mathcal{P} onto \mathcal{B} . The space of probability distributions is not a Euclidean space. Therefore, it is necessary to consider geometry of probability distributions, which is studied in information geometry. It is known that a subspace with linear constraints on natural parameters θ is flat, called e -flat [1, Chapter 2]. The subspace \mathcal{B} is e -flat, meaning that the logarithmic combination, or called e -geodesic, $\mathcal{R} \in \{(1-t) \log \mathcal{Q}_1 + t \log \mathcal{Q}_2 - \phi(t) \mid 0 < t < 1\}$ of any two points $\mathcal{Q}_1, \mathcal{Q}_2 \in \mathcal{B}$ is included in the subspace \mathcal{B} , where $\phi(t)$ is a normalizer. There is always a unique point $\bar{\mathcal{P}}$ on the e -flat subspace that minimizes the KL divergence from any point \mathcal{P} .

$$\bar{\mathcal{P}} = \arg \min_{\mathcal{Q}; \mathcal{Q} \in \mathcal{B}} D_{KL}(\mathcal{P}, \mathcal{Q}). \quad (4)$$

This projection is called the m -projection. The m -projection onto an e -flat subspace is convex optimization. We define two vectors $\boldsymbol{\theta}^B = (\theta_b)_{b \in B}$ and $\boldsymbol{\eta}^B = (\eta_b)_{b \in B}$ and write the dimensionality of these vectors as $|B|$ since it is equal to the cardinality of B . The derivative of the KL divergence and the Hessian matrix $G \in \mathbb{R}^{|B| \times |B|}$ are given as

$$\frac{\partial}{\partial \boldsymbol{\theta}^B} D_{KL}(\mathcal{P}, \mathcal{Q}) = \boldsymbol{\eta}^B - \hat{\boldsymbol{\eta}}^B, \quad \mathbf{G}_{u,v} = \eta_{\max(i_1,j_1),\dots,\max(i_D,j_D)} - \eta_{i_1,\dots,i_D} \eta_{j_1,\dots,j_D}, \quad (5)$$

where $\boldsymbol{\eta}^B$ and $\hat{\boldsymbol{\eta}}^B$ are the expectation parameters of \mathcal{Q} and \mathcal{P} , respectively, and $u = (i_1, \dots, i_D), v = (j_1, \dots, j_D) \in B$. This matrix \mathbf{G} is also known as the negative Fisher information matrix. Using gradient descent with second-order derivative, we can update $\boldsymbol{\theta}^B$ in each iteration t as

$$\boldsymbol{\theta}_{t+1}^B = \boldsymbol{\theta}_t^B - \mathbf{G}^{-1}(\boldsymbol{\eta}_t^B - \hat{\boldsymbol{\eta}}^B). \quad (6)$$

The distribution \mathcal{Q}_{t+1} is calculated from the updated natural parameters $\boldsymbol{\theta}_{t+1}$. This step finds a point $\mathcal{Q}_{t+1} \in \mathcal{B}$ that is closer to the destination \mathcal{P} along with the ϵ -geodesic from \mathcal{Q}_t to \mathcal{P} . We can also calculate the expected value parameters $\boldsymbol{\eta}_{t+1}$ from the distribution. By repeating this process until convergence, we can always find the globally optimal solution satisfying Equation (4). See Section A in Supplement for more detail on the optimization. The problem of how to design and interpret B has not been explored before, and we firstly give the reasoning of B as the presence or absence of particular interactions between modes, which naturally leads to the design guideline of B . The computational complexity of Legendre decomposition is $\mathcal{O}(\gamma|B|^3)$, where γ is the number of iterations.

2.2 Interaction and its representation of tensors

In this subsection, we introduce interactions between modes and its visual representation to prepare for many-body approximation. The following discussion enables us to intuitively describe relationships between modes and formulate our novel rank-free tensor decomposition.

First we introduce n -body parameters, which is a generalized concept of one-body and two-body parameters in [11]. In any n -body parameter, there are n non-one indices; for example, $\theta_{1,2,1,1}$ is a one-body parameter, $\theta_{4,3,1,1}$ is a two-body parameter, and $\theta_{1,2,4,3}$ is a three-body parameter. We also use the following notation for n -body parameters:

$$\theta_{i_k}^{(k)} = \theta_{1,\dots,1,i_k,1,\dots,1}, \quad \theta_{i_k, i_m}^{(k,m)} = \theta_{1,\dots,1,i_k,1,\dots,1,i_m,1,\dots,1}, \quad \theta_{i_k, i_m, i_p}^{(k,m,p)} = \theta_{1,\dots,i_k,\dots,i_m,\dots,i_p,\dots,1},$$

for $n = 1, 2$ and 3 , respectively. We write the energy function \mathcal{H} with n -body parameters as

$$\mathcal{H}_{i_1, \dots, i_D} = H_0 + \sum_{m=1}^D H_{i_m}^{(m)} + \sum_{m=1}^D \sum_{k=1}^{m-1} H_{i_k, i_m}^{(k,m)} + \sum_{m=1}^D \sum_{k=1}^{m-1} \sum_{p=1}^{k-1} H_{i_p, i_k, i_m}^{(p,k,m)} + \dots + H_{i_1, \dots, i_D}^{(1, \dots, D)}, \quad (7)$$

where the n -th order energy is introduced as

$$H_{i_{l_1}, \dots, i_{l_n}}^{(l_1, \dots, l_n)} = - \sum_{i'_{l_1}=2}^{i_{l_1}} \dots \sum_{i'_{l_n}=2}^{i_{l_n}} \theta_{i'_{l_1}, \dots, i'_{l_n}}^{(l_1, \dots, l_n)}. \quad (8)$$

For simplicity, we suppose that $1 \leq l_1 < l_2 < \dots < l_n \leq D$ holds. We set $H_0 = -\theta_{1,\dots,1}$. We say that an n -body interaction exists between modes l_1, \dots, l_n if there are indices i_{l_1}, \dots, i_{l_n} satisfying $H_{i_{l_1}, \dots, i_{l_n}}^{(l_1, \dots, l_n)} \neq 0$. The first term H_0 in Equation (7) is called the normalized factor or the partition function. The terms $H^{(k)}$ are called bias in machine learning and magnetic field or self-energy in statistical physics. The terms $H^{(k,m)}$ are called the weight of the Boltzmann machine in machine learning and two-body interaction or electron-electron interaction in physics.

To visualize the existence of interactions within a tensor, we newly introduce a diagram called *interaction representation*, which is inspired by factor graphs in graphical modelling [4, Chapter 8]. The graphical representation of the product of tensors is widely known as tensor networks. However, displaying the relations between modes of a tensor as a factor graph is our novel approach. We represent the n -body interaction as a black square, \blacksquare , connected with n modes. We describe examples of the two-body interaction between modes (k, m) and the three-body interaction among modes (k, m, p) in Figure 1(a). Combining these interactions, the diagram for the energy function including all two-body interactions is shown in Figure 1(b), and including all two-body and three-body interactions is shown in Figure 1(c) for $D = 4$. This visualization allows us to intuitively understand the relationship between modes of tensors. For simplicity, we abbreviate one-body interactions in the diagrams, while we always assume them. Once interaction representation is given, we can determine the corresponding decomposition of tensors.

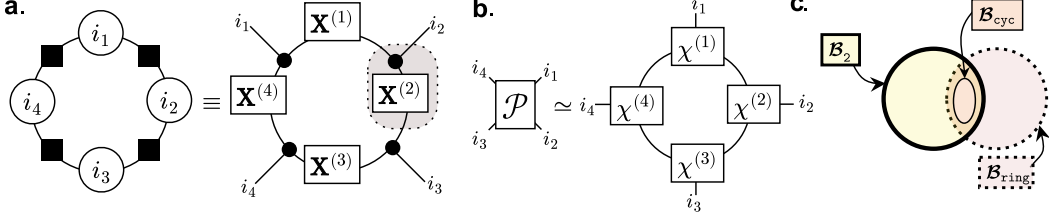


Figure 2: (a)(left) Interaction representation of an example of cyclic two-body approximation and (a)(right) its transformed tensor network for $D = 4$. Each tensor is enclosed by a square and each mode is enclosed by a circle. A black circle \bullet is a hyper diagonal tensor. Edges through \blacksquare between modes mean interaction existence. (b) Tensor network of tensor ring decomposition. (c) The relationship among solution spaces of tensor-ring decomposition $\mathcal{B}_{\text{ring}}$, two-body approximation \mathcal{B}_2 , and cyclic two-body approximation \mathcal{B}_{cyc} .

In Boltzmann machines, we usually consider binary (two-level) variables and their 2nd-order interactions. In our proposal, we consider multi-level D variables, each of which can take a natural number from 1 to I_d for $d \in [D]$. Moreover, higher-order interactions among them are allowed. Therefore our proposal is a form of a multi-level extension of Boltzmann machines with higher-order interaction, where each node of Boltzmann machines corresponds to the tensor mode. In the following section, we reduce some of n -body interactions, that is, $H_{i_1, \dots, i_n}^{(l_1, \dots, l_n)} = 0$, by fixing each parameter $\theta_{i_1, \dots, i_n}^{(l_1, \dots, l_n)} = 0$ for all indices $(i_1, \dots, i_n) \in \{2, \dots, I_1\} \times \dots \times \{2, \dots, I_n\}$.

2.3 Many-body approximation

We approximate a given tensor with assuming the existence of dominant interactions between the modes of the tensor and ignoring other interactions. Since this operation can be understood as enforcing some natural parameters of the distribution to be zero, it can be achieved by convex optimization through the theory of Legendre decomposition. We discuss how we can choose dominant interactions in Section 3.1.

As an example, we consider two types of approximations of a nonnegative tensor \mathcal{P} by tensors represented in Figure 1(b, c). If all energies greater than 2nd-order or those greater than 3rd-order in Equation (7) are ignored, that is, $H_{i_1, \dots, i_n}^{(l_1, \dots, l_n)} = 0$ for $n > 2$ or $n > 3$, $\mathcal{P}_{i_1, i_2, i_3, i_4}$ is approximated as follows:

$$\begin{aligned} \mathcal{P}_{i_1, i_2, i_3, i_4} &\simeq \mathcal{P}_{i_1, i_2, i_3, i_4}^{\leq 2} = \mathbf{X}_{i_1, i_2}^{(1,2)} \mathbf{X}_{i_1, i_3}^{(1,3)} \mathbf{X}_{i_1, i_4}^{(1,4)} \mathbf{X}_{i_2, i_3}^{(2,3)} \mathbf{X}_{i_2, i_4}^{(2,4)} \mathbf{X}_{i_3, i_4}^{(3,4)}, \\ \mathcal{P}_{i_1, i_2, i_3, i_4} &\simeq \mathcal{P}_{i_1, i_2, i_3, i_4}^{\leq 3} = \chi_{i_1, i_2, i_3}^{(1,2,3)} \chi_{i_1, i_2, i_4}^{(1,2,4)} \chi_{i_1, i_3, i_4}^{(1,3,4)} \chi_{i_2, i_3, i_4}^{(2,3,4)}, \end{aligned}$$

where each of matrices and tensors on the right-hand side is represented as

$$\begin{aligned} \mathbf{X}_{i_k, i_m}^{(k, m)} &= \frac{1}{\sqrt[6]{Z}} \exp \left(\frac{1}{3} H_{i_k}^{(k)} + H_{i_k, i_m}^{(k, m)} + \frac{1}{3} H_{i_m}^{(m)} \right), \\ \chi_{i_k, i_m, i_p}^{(k, m, p)} &= \frac{1}{\sqrt[4]{Z}} \exp \left(\frac{H_{i_k}^{(k)}}{3} + \frac{H_{i_m}^{(m)}}{3} + \frac{H_{i_p}^{(p)}}{3} + \frac{1}{2} H_{i_k, i_m}^{(k, m)} + \frac{1}{2} H_{i_m, i_p}^{(m, p)} + \frac{1}{2} H_{i_k, i_p}^{(k, p)} + H_{i_k, i_m, i_p}^{(k, m, p)} \right). \end{aligned}$$

The partition function, or the normalization factor, is given as $Z = \exp(-\theta_{1,1,1,1})$, which does not depend on indices (i_1, i_2, i_3, i_4) . Each $\mathbf{X}^{(k, m)}$ (resp. $\chi^{(k, m, p)}$) is a factorized representation for the relationship between k -th and m -th (resp. k -th, m -th and p -th) modes. Although our model can be transformed into a linear model by taking the logarithm, our convex formulation enables us to find the optimal solution more stable than traditional linear low-rank based nonconvex approaches. Since we do not impose any low-rankness, factorized representations, e.g., $\mathbf{X}^{(k, m)}$ and $\chi^{(k, m, p)}$, can be full-rank matrices or tensors.

For a given tensor \mathcal{P} , we define its m -body approximation $\mathcal{P}^{\leq m}$ as the optimal solution of Equation (4), that is, $\mathcal{P}^{\leq m} = \arg \min_{\mathcal{Q} \in \mathcal{B}} D_{KL}(\mathcal{P}, \mathcal{Q})$, where \mathcal{B} used in \mathcal{B} contains all the indices of $n (\leq m)$ -body parameters. Note that $\mathcal{P}^{\leq D} = \mathcal{P}$ always holds. For any natural number $n < D$, it holds that $\mathcal{B}_n \subseteq \mathcal{B}_{n+1}$, where \mathcal{B}_n is the solution space of n -body approximations. Interestingly,

the two-body approximation for a non-negative tensor with $I_1 = \dots = I_D = 2$ is equivalent to approximating the empirical distribution with the fully connected Boltzmann machine.

In the above discussion, we consider many-body approximation with all the n -body parameters, while we can relax this constraint and allow the use of only a part of n -body parameters in approximation. Let us consider the situation where only one-body interaction and two-body interaction between modes $(d, d+1)$ exist for all $d \in [D]$ ($D+1$ implies 1 for simplicity). Figure 2(a) shows the interaction representation of the approximated tensor. As we can confirm by substituting 0 for $H_{i_k, i_l}^{(k, l)}$ if $l \neq k+1$, we can describe the approximated tensor as

$$\mathcal{P}_{i_1, \dots, i_D} \simeq \mathcal{P}_{i_1, \dots, i_D}^{\text{cyc}} = \mathbf{X}_{i_1, i_2}^{(1)} \mathbf{X}_{i_2, i_3}^{(2)} \dots \mathbf{X}_{i_D, i_1}^{(D)}, \quad (9)$$

where

$$\mathbf{X}_{i_k, i_{k+1}}^{(k)} = \frac{1}{\sqrt{Z}} \exp \left(\frac{1}{2} H_{i_k}^{(k)} + H_{i_k, i_{k+1}}^{(k, k+1)} + \frac{1}{2} H_{i_{k+1}}^{(k+1)} \right)$$

with the normalization factor $Z = \exp(-\theta_{1, \dots, 1})$. When the tensor \mathcal{P} is approximated by \mathcal{P}^{cyc} , the set \mathcal{B} contains only all one-body parameters and two-body parameters $\theta_{i_d, i_{d+1}}^{(d, d+1)}$ for $d \in [D]$. We call this approximation *cyclic two-body approximation* since the order of indices in Equation (9) is cyclic. It holds that $\mathcal{B}_{\text{cyc}} \subseteq \mathcal{B}_2$ for the solution space of cyclic two-body approximation \mathcal{B}_{cyc} (Figure 2(c)).

2.4 Connection to tensor networks

Our tensor interaction representation is an undirected graph that focuses on the relationship between modes. In contrast, tensor networks, which are well known as diagrams that focus on smaller tensors after decomposition, represent a tensor as an undirected graph, whose nodes correspond to matrices or tensors and edges to summation over a mode in tensor products [6].

We provide examples in our representation that can be converted to tensor networks, which implies a tight connection between our representation and tensor networks. For the conversion, we use a hyper-diagonal tensor \mathcal{I} defined as $\mathcal{I}_{ijk} = \delta_{ij} \delta_{jk} \delta_{ki}$, where $\delta_{ij} = 1$ if $i = j$ and 0 otherwise. The tensor \mathcal{I} is often represented by \bullet in tensor networks. In the community of tensor networks, the tensor \mathcal{I} appears in the CNOT gate and a special case of the Z spider [30]. The tensor network in Figure 2(a) represents Equation (9) for $D = 4$.

A remarkable finding is that the converted tensor network representation of cyclic two-body approximation and the tensor network of tensor ring decomposition, whose tensor network is shown in Figure 2(b), have the similar structure in common, despite their different modeling. If we consider the region enclosed by the dotted line in Figure 2(a) as a new tensor, the tensor network of the cyclic two-body approximation coincides with the tensor network of the tensor ring decomposition shown in Figure 2(b). This operation, in which multiple tensors are regarded as a new tensor in a tensor network, is called coarse-graining transformation [9].

Formally, cyclic two-body approximation coincides with tensor ring decomposition with a specific constraint as described below. Non-negative tensor ring decomposition approximates a given tensor $\mathcal{P} \in \mathbb{R}_{\geq 0}^{I_1 \times \dots \times I_D}$ with D core tensors $\chi^{(1)}, \dots, \chi^{(D)} \in \mathbb{R}_{\geq 0}^{R_{d-1} \times I_d \times R_d}$ as

$$\mathcal{P}_{i_1, \dots, i_D} \simeq \sum_{r_1=1}^{R_1} \dots \sum_{r_D=1}^{R_D} \chi_{r_D, i_1, r_1}^{(1)} \dots \chi_{r_{D-1}, i_D, r_D}^{(D)}, \quad (10)$$

where (R_1, \dots, R_D) is called tensor ring rank. The cyclic two-body approximation also approximates the tensor \mathcal{P} in the form of Equation (10), imposing an additional constraint that each core tensor $\chi^{(d)}$ is decomposed as

$$\chi_{r_{d-1}, i_d, r_d}^{(d)} = \sum_{m_d=1}^{I_d} \mathbf{X}_{r_{d-1}, m_d}^{(d)} \mathcal{I}_{m_d, i_d, r_d} \quad (11)$$

for each $d \in [D]$. We assume $r_0 = r_D$ for simplicity. We obtain Equation (9) by substituting Equation (11) into Equation (10).

This constraint enables us to perform convex optimization. This means that we find a subclass \mathcal{B}_{cyc} that can be solved by convex optimization in tensor ring decomposition, which has suffered from the difficulty of non-convex optimization. In addition, this is simultaneously a subclass of two-body approximation as shown in Figure 2(c).

From Kronecker's delta δ , $r_d = i_d$ holds in Equation (11), thus $\chi^{(d)}$ is a tensor with the size (I_{d-1}, I_d, I_d) . Tensor ring rank after the cyclic two-body approximation is (I_1, \dots, I_D) since the size of core tensors coincides with tensor ring rank. This result firstly reveals the relationship between Legendre decomposition and low-rank approximation via tensor networks.

Here we compare the number of parameters of cyclic two-body approximation and that of tensor ring decomposition. The number of elements of an input tensor is $I_1 I_2 \dots I_D$. After cyclic two-body approximation, the number $|B|$ of parameters is given as

$$|B| = 1 + \sum_{d=1}^D (I_d - 1) + \sum_{d=1}^D (I_d - 1)(I_{d+1} - 1), \quad (12)$$

where we assume $I_{D+1} = I_1$. The first term is for the normalizer, the second for the number of one-body parameters, and the final term for the number of two-body parameters. In contrast, in the tensor ring decomposition with the target rank (R_1, \dots, R_D) , the number of parameters is given as $\sum_{d=1}^D R_d I_d R_{d+1}$. The ratio of the number of parameters of these two methods is proportional to I/R^2 if we assume $R_d = R$ and $I_d = I$ for all $d \in [D]$ for simplicity. Therefore, when the target rank is small and the size of the input tensor is large, the proposed method has more parameters than the tensor ring decomposition. The correspondence of many-body approximation to existing low-rank approximation is not limited to tensor ring decomposition. We also provide another example of the correspondence for tensor tree decomposition in Section B.1 in Supplement.

2.5 Many-body approximation as generalization of mean-field approximation

It has been already known that any tensor \mathcal{P} can be represented by vectors $\mathbf{x}^{(1)}, \dots, \mathbf{x}^{(D)} \in \mathbb{R}^{I_d}$ as $\mathcal{P}_{i_1, \dots, i_D} = x_{i_1}^{(1)} x_{i_2}^{(2)} \dots x_{i_D}^{(D)}$ if and only if all $n(\geq 2)$ -body θ -parameters are 0 [10, 12]. The right-hand side is equal to the Kronecker product of D vectors $\mathbf{x}^{(1)}, \dots, \mathbf{x}^{(D)}$, and therefore this approximation is equivalent to the rank-1 approximation since the rank of the tensor that can be represented by the Kronecker product is always 1, which is also known to correspond to mean-field approximation. In this study, we propose many-body approximation by relaxing the condition for the mean-field approximation that ignores $n(\geq 2)$ -body interactions. Therefore many-body approximation is generalization of rank-1 approximation and mean-field approximation.

3 Experiments

We conduct three experiments to see the usefulness and effectiveness of many-body approximation. Datasets and implementation details are available in Supplement.

3.1 An example for tuning interaction

We extract ten color images from Columbia Object Image Library (COIL-100) [29] and construct a tensor $\mathcal{P} \in \mathbb{R}_{\geq 0}^{40 \times 40 \times 3 \times 10}$, where each mode represents the width, height, color, or image index, respectively. Then we decompose \mathcal{P} with varying chosen interactions and show the reconstructed images. Figure 3(a) shows $\mathcal{P}^{\leq 4}$, which coincides with the input tensor \mathcal{P} itself since its order is four. Reconstruction quality gradually drops when we reduce interactions from Figure 3(a) to Figure 3(d). We can explicitly control the trend of reconstruction by manually choosing interaction, which is one of characteristics of the proposal. In Figure 3(c), each reconstructed image has a monotone taste because the color is not directly interacted with the pixel position (width and height). In Figure 3(d), although the whole tensor is monotone because the color is independent of any other modes, the reconstruction keeps the objects' shapes since the interaction among width, height, and image index are still kept. See Figure 7 in Supplement for the role of the interaction. Interactions between modes are interpretable, which is in contrast to the rank of tensors that is often difficult to interpret. Therefore, tuning of interactions is more intuitive than that of ranks.

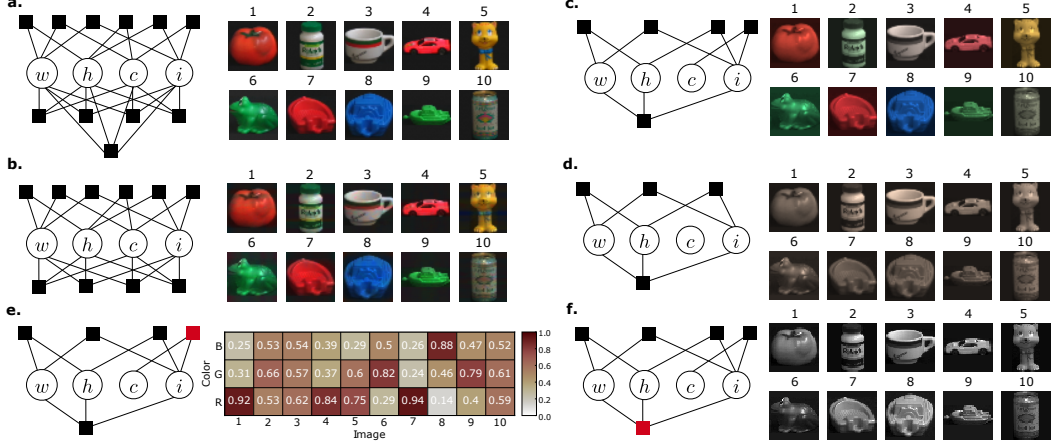


Figure 3: (a,b) Four-body and three-body approximation for the COIL dataset. (c,d) Appropriate selection of interactions controls the richness of color. Visualization of interaction between (e) color and image index, and (f) width, height, and image index.

Table 1: Recovery fit score for tensor completion.

	Scenario 1	Scenario 2	Scenario 3
LBTC	0.948 ± 0.00152	0.917 ± 0.000577	0.874 ± 0.00153
HaLRTC	0.864	0.842	0.825
SiLRTC	0.863	0.841	0.820
SiLRTCTT	0.948	0.915	0.868
PTRCRW	0.945 ± 0.0000	0.901 ± 0.0000	0.844 ± 0.0000

We also visualize the interaction between color and image as a heatmap of a matrix $\mathbf{X}^{(c,i)} \in \mathbb{R}^{3 \times 10}$ in Figure 3(e), which is obtained in the case of Figure 3(c). We normalize each column of $\mathbf{X}^{(c,i)}$ with the L2 norm for better visualization. As expected, indices corresponding to red objects (i.e., 1, 4, and 7) have large values in the third red-color row. We also visualize the interaction among width, height, and image index, which corresponds to a tensor $\chi^{(w,h,i)} \in \mathbb{R}^{40 \times 40 \times 10}$ without any information of colors, as a series of heatmaps in Figure 3(f). They provide the gray-scale reconstruction of images. The above discussion implies that many-body approximation captures patterns or features of inputs.

3.2 Tensor completion by many-body approximation

Since our proposal is an alternative to the existing low-rank approximation, we can replace it with our many-body approximation in practical applications. As a representative application, we demonstrate missing value estimation by the *em*-algorithm [28], where we replace the *m*-step of low-rank approximation with many-body approximation. We call this approach Low-Body Tensor Completion (LBTC). See Algorithm 2 in Supplement for its pseudo-code.

To examine the performance of LBTC, we have conducted experiments on a real-world dataset, the traffic speed dataset in District 7, Los Angeles County, collected from PeMS [34]. This data was obtained from fixed-point observations of vehicle speeds every 5 minutes for 28 days. We made $28 \times 24 \times 12 \times 4$ tensor \mathcal{T} , whose modes correspond to date, hour, minute, and lane. As practical situations, we assume that a disorder of a lane's speedometer causes random and continuous deficiencies. We prepared three patterns of missing cases: a case with a disorder in the speedometer in lane 1 (scenario 1), a case with disorders in the speedometers in lanes 1, 2, and 3 (scenario 2), and a case with disorders in all speedometers (scenario 3). The missing rates for scenarios 1, 2, and 3 were 9%, 27%, and 34%, respectively. We evaluate the recovery fit score $1 - \|\mathcal{T}_\tau - \bar{\mathcal{T}}_\tau\|_F / \|\mathcal{T}_\tau\|_F$ for the reconstruction $\bar{\mathcal{T}}$ and missing indices τ .

In the proposal, we need to choose interactions to use. Intuitively, the interaction between date and minute and that between minute and lane seem irrelevant. Therefore, we used all the two-body

interactions except for the above two interactions. In addition, the interaction among date, hour, and minute is also included because it is intuitively relevant.

As baseline methods, we use SiLRTC, HaLRTC [21], SiLRTC-TT [3], and PTRCRW [42]. SiLRTC-TT and PTRCRW are based on tensor train and ring decompositions, respectively, and PTRCRW is known as state-of-the-art. The reconstructions are available in Figure 8 in Supplement with ground truth. We tuned hyperparameters of baseline methods and compared their best results with LBTC. Resulting scores in Table 1 show that our method is superior to other methods. Moreover, we can intuitively tune interactions in the proposal, while other baselines need typical hyperparameter tuning as seen in Figure 14 in Supplement. In our method, interactions among non-associated modes could worsen the performance as seen in Table 2 in Supplement. Since the proposal and PTRCRW are non-convex optimization, we run each of them 10 times with random initialization and report mean values and the standard error. Note that many-body approximation itself is always convex, while our tensor completion algorithm LBTC is non-convex due to the use of the *em*-algorithm.

3.3 Comparison with ring decomposition

As seen in Section 2.4, many-body approximation has a close connection to low-rank approximation. For example, in tensor ring decomposition, if we impose the constraint that decomposed smaller tensors can be represented as products with hyper-diagonal tensors \mathcal{I} , this decomposition is equivalent to a cyclic two-body approximation. Therefore, to examine our conjecture that cyclic two-body approximation is as capable of approximating as tensor ring decomposition, we empirically examine the effectiveness of cyclic two-body approximation compared with tensor ring decomposition. As baselines, we use five existing methods of non-negative tensor ring decomposition, NTR-APG, NTR-HALS, NTR-MU, NTR-MM and NTR-IraMM [43, 44]. We also describe the efficiency in Supplement.

We evaluate the approximation performance by the relative error $\|\mathcal{T} - \bar{\mathcal{T}}\|_F / \|\mathcal{T}\|_F$ for an input tensor \mathcal{T} and a reconstructed tensor $\bar{\mathcal{T}}$. Since all the existing methods are based on nonconvex optimization, we plot the best score (minimum relative error) among 5 restarts with random initialization. In contrast, the score of our method is obtained by a single run as it is convex optimization and such restarts are fundamentally unnecessary.

Synthetic data We performed experiments on two synthetic datasets with low tensor ring rank. We create 6th and 7th-order tensors with ring ranks (15, ..., 15) and (10, ..., 10), respectively. Relative error are plotted with gradually increasing the target rank of the tensor ring decomposition, which is compared to the score of our method, plotted as the cross point of horizontal and vertical red dotted lines. Please note that our method does not have the concept of the rank, thus the score of our method is invariant to changes of the target rank unlike other methods. If the cross point of red dotted lines is lower than other lines, the proposed method is better than other methods. In both experiments, the proposed method is superior to comparison partners in terms of the reconstruction error.

Real data Next, we evaluate our method on real data. TT_ChartRes and TT_Origami are 7-order tensors, which are produced from TokyoTech Hyperspectral Image Dataset [24, 25]. Each tensor has been reshaped to reduce the computational complexity. As seen in Figure 4, the proposed method keeps the competitive relative errors. In baselines, a slight change of the target rank can induce a significant increase of the reconstruction error due to the nonconvexity. These results mean that we eliminate the instability of non-negative tensor ring decomposition by our convex formulation.

4 Conclusion

We propose *many-body approximation* for tensors, which decomposes tensors with focusing on the relationship between modes represented by an energy-based model. It approximates and regularizes tensors by ignoring the energy corresponding to certain interactions, which can be viewed as

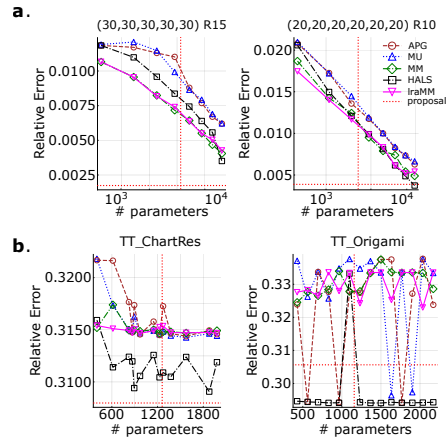


Figure 4: Experimental results for real datasets. The vertical red dotted line is $|B|$ (See Equation (12)).

a generalized formulation of mean-field approximation that considers only one-body interactions. Our novel formulation enables us to achieve convex optimization of the model, while the existing approaches based on the low-rank structure are non-convex and empirically unstable with respect to the rank selection. Furthermore, we introduce a way of visualizing interactions between modes, called interaction representation, to see activated interactions between modes. We have demonstrated transformation between our representation and tensor networks, which reveals the nontrivial connection between many-body approximation and the classical tensor low-rank tensor decomposition. We have empirically showed the intuitive model’s designability and the better usefulness in tensor completion and approximation tasks compared to baseline methods.

Limitation Proposal works on only non-negative tensors. We have examined the effectiveness of LBTC on only traffic datasets.

A Projection theory in information geometry

We explain concepts of information geometry used in this study, including natural parameters, expectation parameters, model flatness, and convexity of optimization. In the following discussion, we consider only discrete probability distributions.

(θ, η) -coordinate and geodesics In this study, we treat a normalized D -order non-negative tensor $\mathcal{P} \in \mathbb{R}_{\geq 0}^{I_1 \times \dots \times I_D}$ as a discrete probability distribution with D random variables. Let \mathcal{U} be the set of discrete probability distributions with D random variables. The entire space \mathcal{U} is a non-Euclidean space with the Fisher information matrix \mathbf{G} as the metric. This metric measures the distance between two points. In Euclidean space, the shortest path between two points is a straight line. In a non-Euclidean space, such a shortest path is called a geodesic. In the space \mathcal{U} , two kinds of geodesics can be introduced, e -geodesics and m -geodesics. For two points $\mathcal{P}_1, \mathcal{P}_2 \in \mathcal{U}$, e - and m -geodesics are defined as

$$\{ \mathcal{R}_t \mid \log \mathcal{R}_t = (1-t) \log \mathcal{P}_1 + t \log \mathcal{P}_2 - \phi(t) \}, \quad \{ \mathcal{R}_t \mid \mathcal{R}_t = (1-t)\mathcal{P}_1 + t\mathcal{P}_2 \},$$

respectively, where $0 \leq t \leq 1$ and $\phi(t)$ is a normalization factor to keep \mathcal{R}_t to be a distribution.

We can parameterize distributions $\mathcal{P} \in \mathcal{U}$ by parameters called natural parameters. We have described the relationship between a distribution \mathcal{P} and a natural parameter vector $\boldsymbol{\theta} = (\theta_{2,\dots,1}, \dots, \theta_{I_1,\dots,I_D})$ in Equation (1). The natural parameter $\boldsymbol{\theta}$ serves as a coordinate system of \mathcal{U} , since any distribution in \mathcal{U} is specified by determining $\boldsymbol{\theta}$. Furthermore, we can also specify a distribution \mathcal{P} by its expectation parameter vector $\boldsymbol{\eta} = (\eta_{2,\dots,1}, \dots, \eta_{I_1,\dots,I_D})$, which corresponds to expected values of the distribution and an alternative coordinate system of \mathcal{U} . The definition of the expectation parameter $\boldsymbol{\eta}$ is described in Equation (3). θ -coordinates and η -coordinates are orthogonal with each other, which means that the Fisher information matrix \mathbf{G} has the following property, $\mathbf{G}_{u,v} = \partial \eta_u / \partial \theta_v$ and $(\mathbf{G}^{-1})_{u,v} = \partial \theta_u / \partial \eta_v$. e - and m -geodesics can also be described using these parameters as follows.

$$\{ \boldsymbol{\theta}^t \mid \boldsymbol{\theta}^t = (1-t)\boldsymbol{\theta}^{\mathcal{P}_1} + t\boldsymbol{\theta}^{\mathcal{P}_2} \}, \quad \{ \boldsymbol{\eta}^t \mid \boldsymbol{\eta}^t = (1-t)\boldsymbol{\eta}^{\mathcal{P}_1} + t\boldsymbol{\eta}^{\mathcal{P}_2} \},$$

where $\boldsymbol{\theta}^{\mathcal{P}}$ and $\boldsymbol{\eta}^{\mathcal{P}}$ are θ - and η -coordinate of a distribution $\mathcal{P} \in \mathcal{U}$.

Flatness and projections A subspace is called e -flat when any e -geodesic connecting two points in a subspace is included in the subspace. The vertical descent of an m -geodesic from a point $\mathcal{P} \in \mathcal{U}$ onto e -flat subspace \mathcal{B}_e is called m -projection. Similarly, e -projection is obtained when we replace all e with m and m with e . The flatness of subspaces guarantees the uniqueness of the projection destination. The projection destination $\bar{\mathcal{P}}$ or $\tilde{\mathcal{P}}$ obtained by m - or e -projection onto \mathcal{B}_e or \mathcal{B}_m minimizes the following KL divergence,

$$\bar{\mathcal{P}} = \arg \min_{\mathcal{Q} \in \mathcal{B}_e} D_{KL}(\mathcal{P}, \mathcal{Q}), \quad \tilde{\mathcal{P}} = \arg \min_{\mathcal{Q} \in \mathcal{B}_m} D_{KL}(\mathcal{Q}, \mathcal{P}).$$

The KL divergence from discrete distributions $\mathcal{P} \in \mathcal{U}$ to $\mathcal{Q} \in \mathcal{U}$ is given as

$$D_{KL}(\mathcal{P}, \mathcal{Q}) = \sum_{i_1=1}^{I_1} \dots \sum_{i_D=1}^{I_D} \mathcal{P}_{i_1, \dots, i_D} \log \frac{\mathcal{P}_{i_1, \dots, i_D}}{\mathcal{Q}_{i_1, \dots, i_D}}. \quad (13)$$

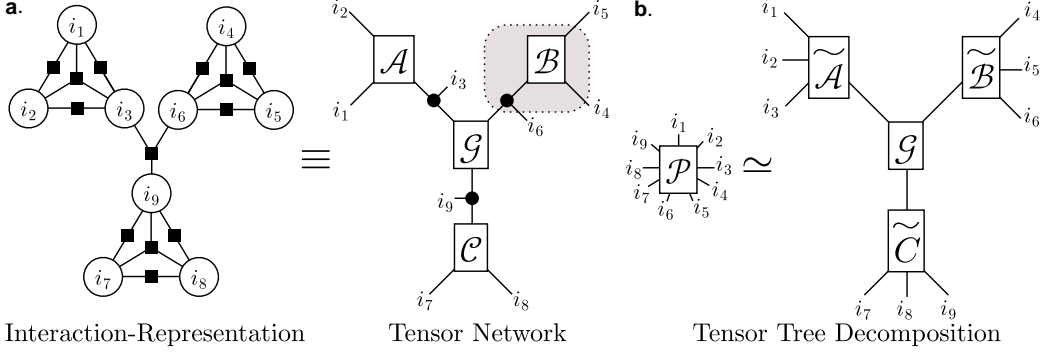


Figure 5: (a) Interaction representation corresponding to Equation (14) and its transformed tensor network for $D = 9$. (b) Tensor network of a variant of tensor tree decomposition.

It is known that a subspace with linear constraints on natural parameters θ is e -flat [1, Chapter 2]. The proposed many-body approximation performs m -projection onto the subspace $\mathcal{B} \subset \mathcal{U}$ with some natural parameters fixed to be 0. From this linear constraint, we know that \mathcal{B} is e -flat. Therefore, the optimal solution of the many-body approximation is always unique. When a space is e -flat and m -flat at the same time, we say that the space is dually-flat. The set of discrete probability distributions \mathcal{U} is dually-flat.

Natural gradient method $e(m)$ -flatness guarantees that cost functions to be optimized in Equation (13) are convex. Therefore, $m(e)$ -projection onto an $e(m)$ -flat subspace can be implemented by a gradient method using a second-order gradient. This second-order gradient method is known as the natural gradient method [2]. The Fisher information matrix \mathbf{G} appears by second-order differentiation of the KL divergence (see Equation (5)). We can perform fast optimization using the update formula in Equation (6), using the inverse of the Fisher information matrix.

Examples for Möbius function In the proposed method, we need to transform the distribution $\mathcal{P} \in \mathbb{R}^{I_1 \times \dots \times I_D}$ with θ and η using the Möbius function, defined in Section 2.1. We provide examples here. In Equation (2), The Möbius function is used to find the natural parameter θ from a distribution \mathcal{P} . For example, if $D = 2, 3$, it holds that

$$\begin{aligned} \theta_{i_1, i_2} &= \log \mathcal{P}_{i_1, i_2} - \log \mathcal{P}_{i_1-1, i_2} - \log \mathcal{P}_{i_1, i_2-1} + \log \mathcal{P}_{i_1-1, i_2-1}, \\ \theta_{i_1, i_2, i_3} &= \log \mathcal{P}_{i_1, i_2, i_3} - \log \mathcal{P}_{i_1-1, i_2, i_3} - \log \mathcal{P}_{i_1, i_2-1, i_3} - \log \mathcal{P}_{i_1, i_2, i_3-1} \\ &\quad + \log \mathcal{P}_{i_1-1, i_2-1, i_3} + \log \mathcal{P}_{i_1, i_2-1, i_3-1} + \log \mathcal{P}_{i_1, i_2-1, i_3-1} - \log \mathcal{P}_{i_1-1, i_2-1, i_3-1}, \end{aligned}$$

where we assume $\mathcal{P}_{0, i_2} = \mathcal{P}_{i_1, 0} = 1$ and $\mathcal{P}_{i_1, i_2, 0} = \mathcal{P}_{i_1, 0, i_3} = \mathcal{P}_{0, i_2, i_3} = 1$. Note that, to identify the value of θ_{i_1, \dots, i_d} , we need only $\mathcal{P}_{i'_1, \dots, i'_d}$ with $(i'_1, \dots, i'_d) \in \{i_1-1, i_1\} \times \{i_2-1, i_2\} \times \dots \times \{i_d-1, i_d\}$. In the same way, using Equation (3), we can find the distribution \mathcal{P} by the expectation parameter η . For example, if $D = 2, 3$, it holds that

$$\begin{aligned} \mathcal{P}_{i_1, i_2} &= \eta_{i_1, i_2} - \eta_{i_1+1, i_2} - \eta_{i_1, i_2+1} + \eta_{i_1+1, i_2+1}, \\ \mathcal{P}_{i_1, i_2, i_3} &= \eta_{i_1, i_2, i_3} - \eta_{i_1+1, i_2, i_3} - \eta_{i_1, i_2+1, i_3} - \eta_{i_1, i_2, i_3+1} \\ &\quad + \eta_{i_1+1, i_2+1, i_3} + \eta_{i_1+1, i_2, i_3+1} + \eta_{i_1, i_2+1, i_3+1} - \eta_{i_1+1, i_2+1, i_3+1}, \end{aligned}$$

where we assume $\eta_{i_1+1, i_2} = \eta_{i_1, i_2+1} = 0$ and $\eta_{i_1+1, i_2, i_3} = \eta_{i_1, i_2+1, i_3} = \eta_{i_1, i_2, i_3+1} = 0$.

B Theoretical remarks

B.1 Another example: Tensor tree decomposition

As seen in Section 2.4, cyclic two-body approximation coincides with tensor ring decomposition with a constraint. In this section, we additionally provide another example of correspondence between many-body approximation and the existing low-rank approximation. For $D = 9$, let us consider three-body and two-body interactions among (i_1, i_2, i_3) , (i_4, i_5, i_6) , and (i_7, i_8, i_9) and three-body

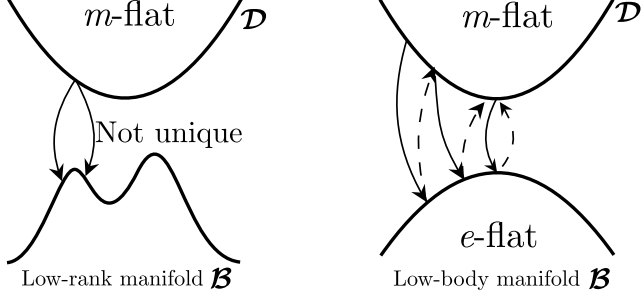


Figure 6: The *em*-algorithm. Dashed(Solid) arrows are $e(m)$ -projection.

approximation among (i_3, i_6, i_9) . We provide the interaction representation of the target energy function in Figure 5(a). In this approximation, the decomposed tensor can be described as

$$\mathcal{P}_{i_1, \dots, i_9} = \mathcal{A}_{i_1, i_2, i_3} \mathcal{B}_{i_4, i_5, i_6} \mathcal{C}_{i_7, i_8, i_9} \mathcal{G}_{i_3, i_6, i_9}. \quad (14)$$

Its converted tensor network is described in Figure 5(a). It becomes a tensor network of tensor tree decomposition in Figure 5(b) when the region enclosed by the dotted line is replaced with a new tensor (shown with tilde) by coarse-graining. Such tensor tree decomposition is used in generative modeling [5], computational chemistry [27] and quantum many-body physics [37].

B.2 Reducing computational complexity by reshaping tensor

As described in Section 2.1.1, the computational complexity of many-body approximation is $\mathcal{O}(\gamma|B|^3)$, where γ is the number of iterations, because the overall complexity is dominated by the update of θ , which includes matrix inversion of \mathbf{G} and the complexity of computing the inverse of an $n \times n$ matrix is $\mathcal{O}(n^3)$. This complexity can be reduced if we reshape tensors so that the size of each mode becomes small. For example, let us consider a 3-order tensor whose size is (J^2, J^2, J^2) and its cyclic two-body approximation. In this case, the time complexity is $\mathcal{O}(\gamma J^{12})$ since it holds that $|B| = \mathcal{O}(J^4)$ (See Equation (12)). In contrast, if we reshape the input tensor to a 6-order tensor whose size is (J, J, J, J, J, J) , the time complexity becomes $\mathcal{O}(\gamma J^6)$ since it holds that $|B| = \mathcal{O}(J^2)$.

This technique of reshaping a tensor into a larger-order tensor is widely used practically in various methods based on tensor networks, such as tensor ring decomposition [23]. We use this technic in the experiment in Section 3.3 to handle large tensors in the both of proposal and baselines.

B.3 Information geometric view of LBTC

Traditional methods for tensor completion are based on the following iteration, called *em*-algorithm [41].

$$\text{e-step: } \mathcal{P}_\Omega \leftarrow \mathcal{T}_\Omega, \quad \text{m-step: } \mathcal{P} \leftarrow \text{low-rank-approximation}(\mathcal{P}),$$

with an initialized tensor \mathcal{P} , where Ω is the set of observed indices of a given tensor \mathcal{T} with missing values. From the information geometric view, *m*-step does *m*-projection onto the model manifold \mathcal{B} consisting of low-rank tensors, and *e*-step does *e*-projection onto the data manifold $\mathcal{D} \equiv \{ \mathcal{P} \mid \mathcal{P}_\Omega = \mathcal{T}_\Omega \}$. It is straightforward to prove that *e*-step finds a point $\bar{\mathcal{P}} = \arg \min_{\bar{\mathcal{P}} \in \mathcal{D}} D_{KL}(\bar{\mathcal{P}}, \mathcal{P})$ for the obtained tensor \mathcal{P} by the previous *m*-step [45]. The iteration of *e*- and *m*-step finds the closest point between two manifolds \mathcal{B} and \mathcal{D} . Since we can immediately prove that $t\mathcal{Q}_1 + (1-t)\mathcal{Q}_2$ belongs to \mathcal{D} for any $\mathcal{Q}_1, \mathcal{Q}_2 \in \mathcal{D}$ and $0 \leq t \leq 1$, the data manifold \mathcal{D} is *m*-flat, which guarantees the uniqueness of the *e*-step. See the definition of *m*-flat in Section A. However, since low-rank subspace is not *e*-flat, that *m*-projection is not unique. LBTC conducts tensor completion by replacing low-rank approximation in *m*-step with many-body approximation. Since the model manifold of many-body approximation is always *e*-flat and data manifold is *m*-flat, each step in the algorithm is unique. Instead of hyper-parameters related to ranks that traditional tensor completion methods require, LBTC requires only information about interactions to be used, but it can be intuitively tuned, as seen in Section 3.1.

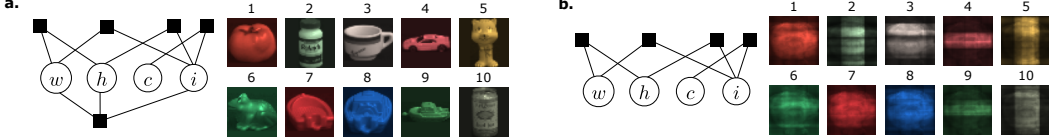


Figure 7: (a) Many-body approximation with three-body interaction among width, height, and index image can reconstruct the shapes of each image. (b) Without the interaction, many-body approximation cannot reconstruct the shapes of each image.

C Additional numerical results

C.1 Additional results for COIL dataset

In Section 3.1, we see that interactions related to color control color-richness in the reconstruction. We provide additional experimental results in Figure 7 to see the role of the interaction among width, height, and image index. The figure shows the influence of the interaction for reconstruction. While Figure 7(b), without the interaction, could not capture the shapes of images, Figure 7(a) reconstruct each shape properly. Based on these results, it is reasonable that the interaction is responsible for these shapes.

C.2 Additional results for LBTC

We provide the reconstructions by the experiments in Section 3.2 in Figure 8 with ground truth.

In traditional low-rank approximation, tuning hyper-parameters based on prior knowledge is difficult because its semantics are unclear. In contrast, the interactions in many-body approximation can be tuned easily by considering the expected correlation among modes of a given tensor. To support this claim, we additionally confirm that LBTC scores get better when we activate interactions between modes that are expected to be correlated based on prior knowledge. In this experiment, we use the same datasets in Section 3.2. We prepare two set of interactions, interaction A and B, as shown on the left in Figure 9. In interaction A, we activate interaction between modes such as (date, hour) and (hour, minute, lane), which we expect to be correlated. In interaction B, we activate interaction between modes such as (date, minute) and (minute, lane), which we do not expect to be correlated. For a fair comparison, we chose these interactions so that the number of parameters used in interactions A and B are as close as possible, where the number of parameters for interaction A was 1847, and the number of parameters for interaction B was 1619. As seen in Table 2, LBTC with interaction A always has a better score than interaction B, which implies that many-body approximation has better performance when we choose interactions among correlated modes. We conducted the experiment 10 times and reported mean values with standard error. We also visualize the reconstruction in Figure 9 to show that LBTC with interaction A can complete tensors more accurately than that with interaction B.

As seen in Figure 14 and Section E.2, existing methods require hyper-parameters that are difficult to tune since we usually cannot find any correspondence between these values and prior knowledge about the given tensor. In contrast, as demonstrated in this section, our energy-based model is intuitively tunable that can skip time-consuming hyper-parameter tuning.

Table 2: Dependency of recovery fit score of LBTC on a choice of interaction.

	Scenario 1	Scenario 2	Scenario 3
Interaction A	0.900 ± 0.00125	0.889 ± 0.000632	0.864 ± 0.001264
Interaction B	0.820 ± 0.00143	0.819 ± 0.000699	0.805 ± 0.000527

C.3 Additional results for comparison with ring decomposition

We additionally provide Figure 10, which shows running time compassion in the experiment in Section 3.3. As described in the main text, we repeat five times each baseline method with random

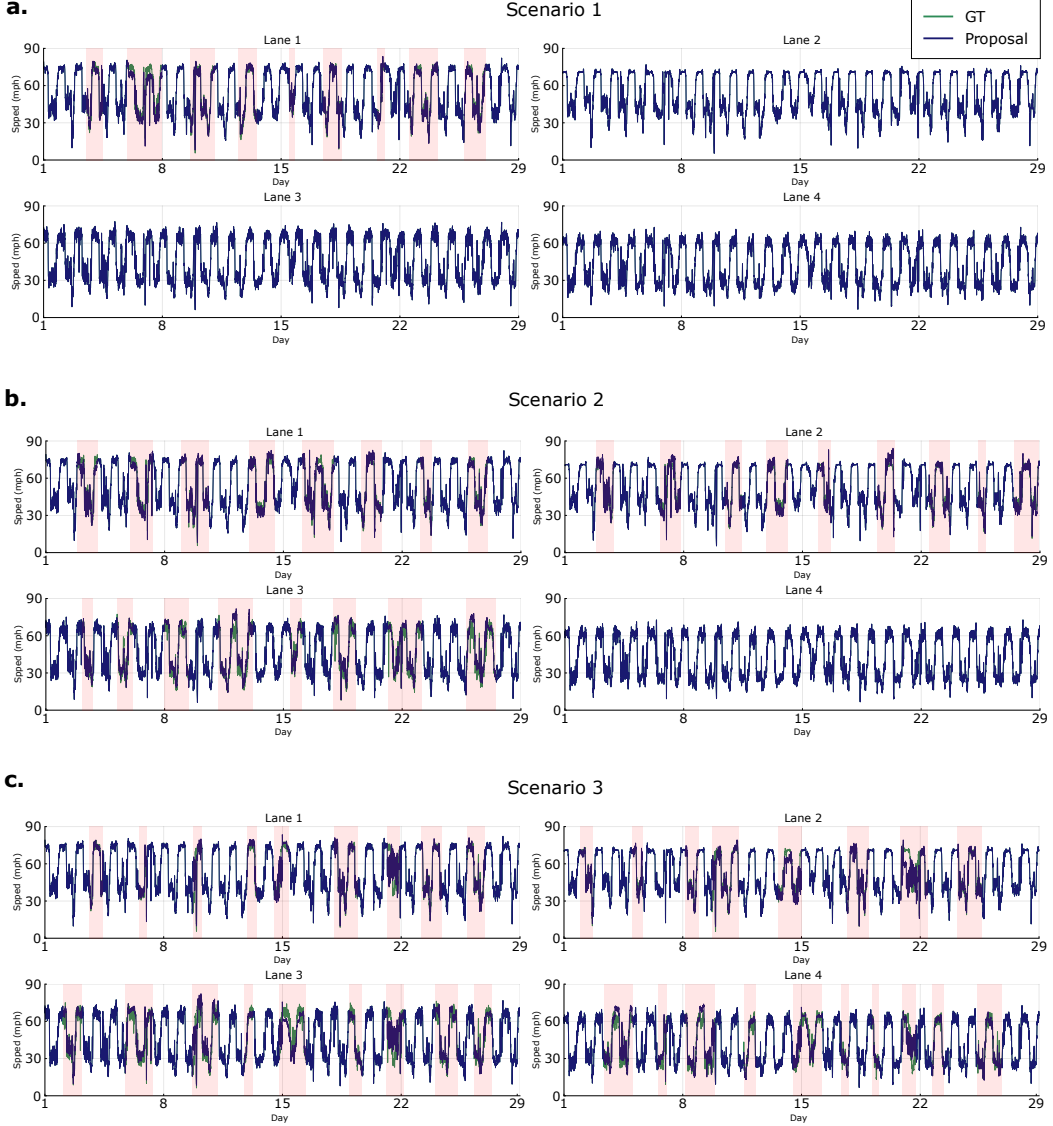


Figure 8: Ground truth and reconstruction by LBTC in the experiment in Section 3.2. Filled areas are missing parts, and blue lines are estimated values by the proposal. Green lines are ground truth.

initialization while the proposal runs only once. We compare the total running time of them. As seen in Figure 10, for both synthetic and real datasets, the proposed method is always faster than baselines, keeping the competitive relative errors. The flatness of solution space enables many-body approximation to be solved with the Newton method. In contrast, NTR is solved by a first-order derivative. The quadratic convergence of the Newton method is well known, and it requires only a few iterations to find the best solution in the flat solution space \mathcal{B}_{cyc} . That is the reason why the proposed method is fast and stable.

C.4 Comparison with traditional low-rank approximation

In low-rank approximation, we often gradually increase the rank to enlarge model capability. In the same way, if we have no prior or domain knowledge about a tensor, we can gradually increase m of m -body approximation and get more accurate reconstruction. To demonstrate that, we conduct additional experiments with the same dataset in Section 3.2. We compare the reconstruction ability of the proposed m -body approximation with non-negative tucker decomposition (NTD) [14] and non-negative tensor train decomposition (NTTF) [36].

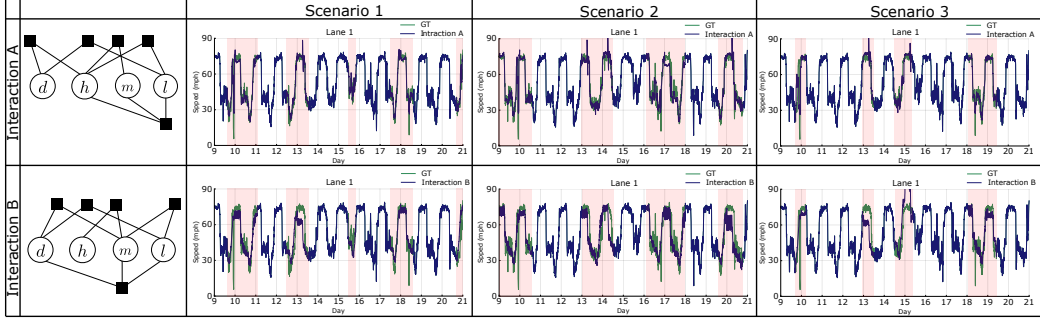


Figure 9: Interaction dependency of LBTC. Filled areas are missing parts, and blue lines are estimated values by the proposal with interaction A and B, respectively. Green lines are ground truth. Due to space limitations, we show the reconstruction of Lane 1 from day 9 to 20, where many missing parts exists.

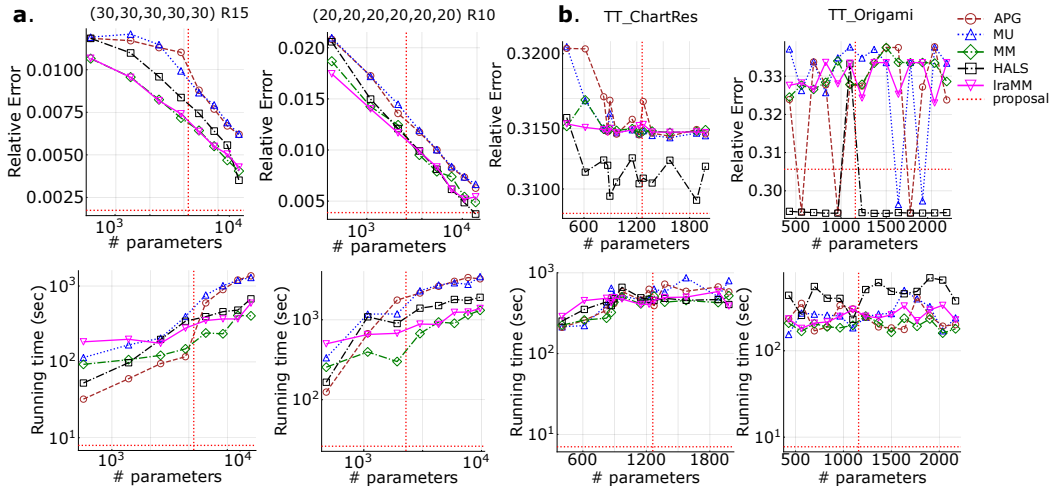


Figure 10: Comparison of reconstruction capabilities (top) and computational speed (bottom) of cyclic two-body approximation and tensor ring decomposition for synthetic low-tensor ring datasets **(a)** and real datasets **(b)**. The vertical red dotted line is $|\mathcal{B}|$ (See Equation (12)).

In many applications based on matrix and tensor factorization, their objective functions are often the fit score (RMSE) and they try to find good representations to solve the task by optimizing the objective. Therefore, for fair evaluation without depending on specific applications, we examine the performance by fit score.

For m -body approximation, we gradually increase the order of the interaction by changing m to 1, 2, 3. We run the proposal only once since the proposal does not depend on initial values. For baselines, we gradually enlarge model capacity by increasing the target rank. We repeat each baseline 20 times with random initialization. We define the Tucker and train ranks for the baseline method in two ways: first, we assume all values in ranks are the same, that is (r, \dots, r) and increase the value of r . However, since the size of an input tensor is $(28, 24, 12, 4)$ and each mode size is not unique, it can be unnatural rank setting, that may cause worse RMSE. To avoid that, we also adjust target rank by taking the tensor size into account. In particular, the rank is set to be $(1, 1, 1, 1)$, $(6, 2, 2, 1)$, $(6, 5, 2, 1)$, $(8, 5, 4, 2)$, $(10, 7, 4, 2)$, $(12, 9, 4, 2)$, $(16, 12, 6, 2)$, $(18, 15, 8, 2)$, $(20, 18, 11, 3)$ for NTD and $(1, 1, 1)$, $(1, 2, 1)$, $(1, 2, 2)$, $(2, 2, 2)$, $(4, 2, 2)$, $(6, 2, 2)$, $(6, 3, 2)$, $(8, 3, 2)$, $(10, 3, 2)$, $(10, 4, 2)$, $(15, 4, 2)$, $(20, 5, 2)$, $(20, 8, 2)$, $(30, 10, 2)$, $(30, 15, 8)$ for NTTF.

We evaluate the approximation performance with the fit score $1 - \|\mathcal{P} - \bar{\mathcal{P}}\|_F / \|\mathcal{P}\|_F$ for the input \mathcal{P} and the reconstructed tensor $\bar{\mathcal{P}}$. We show these results in Figure 11. While baselines are often trapped in a worse local minimum, the proposal reconstructs the original tensor better. We also show

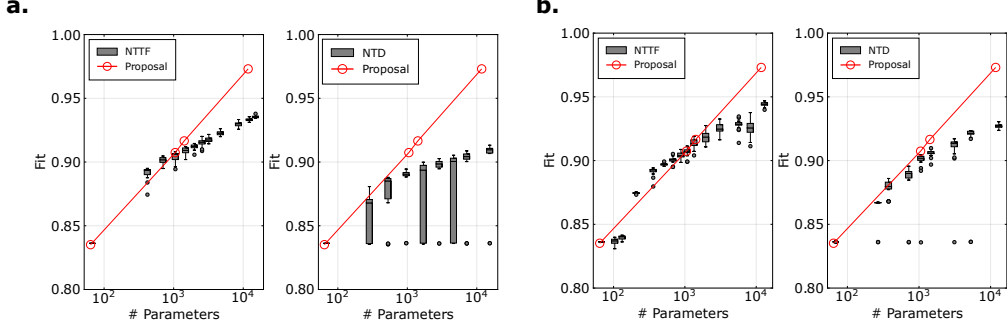


Figure 11: We compare the fit score of proposal $\mathcal{P}^{\leq 1}, \mathcal{P}^{\text{cyc}}, \mathcal{P}^{\leq 2}, \mathcal{P}^{\leq 3}$ with baselines. (a) The ranks for baselines assumed as (r, \dots, r) with changing the value of r . (b) The ranks for baselines are tuned taking into the tensor size account.

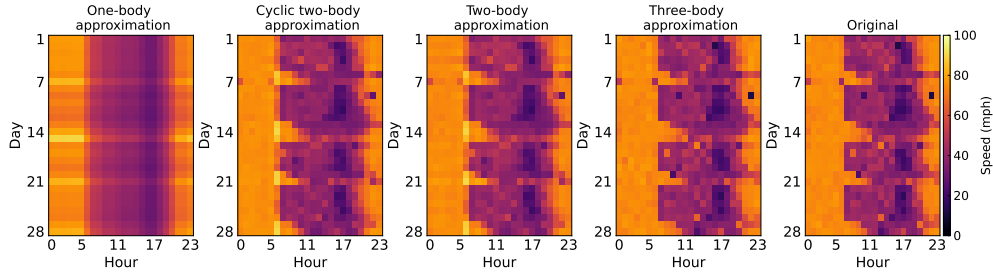


Figure 12: Heatmaps for reconstructed tensor $\mathcal{P}^{\leq 1}, \mathcal{P}^{\text{cyc}}, \mathcal{P}^{\leq 2}, \mathcal{P}^{\leq 3}$ and input tensor \mathcal{P} . We visualize the traffic on only the first lane at 00 minutes every hour, corresponds to $\mathcal{P}[:, :, 1, 1]$.

the reconstruction by the proposed method as heatmaps in Figure 12. Even one-body approximation is able to reconstruct the rush hour around 17:00. When the number of interactions increases, we can observe the trend that the time of the busy hours on weekends are different from those on weekdays more clearly.

To see the effectiveness of proposal for data mining, we additionally plot two-body interaction between day and lane extracted by the two-body approximation of the above traffic data. This is a matrix $\mathbf{X}^{(d,l)} \in \mathbb{R}^{28 \times 4}$. As seen in Figure 13, the value in the first column is always the largest and that in the fourth column is always the smallest. From this result, we can interpret that the data corresponding to $\mathcal{P}[:, :, :, 1]$ were taken in the overtaking lane and the data for $\mathcal{P}[:, :, :, 4]$ were taken in the overtaken lane.

D Dataset details

We describe the details of each dataset in the following.

D.1 For experiment with RGB images.

We downloaded the COIL-100 dataset from the official web page¹. We used ten images with object numbers 4, 5, 7, 10, 17, 23, 28, 38, 42 and 78. This selection aimed to include both monochromatic and multi-colored objects so that we can see how the proposed method changes the reconstruction if we deactivate the interactions related to color. We reshaped the size of each image to 40×40 .

¹<https://www1.cs.columbia.edu/CAVE/software/softlib/coil-100.php>

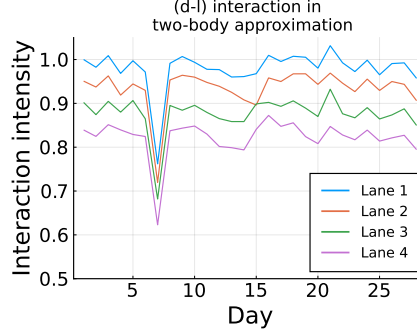


Figure 13: The obtained interaction between day and lane in two-body approximation.

D.2 For experiments with LRTC

We downloaded traffic speed records in District 7, Los Angeles County, from PeMS². The data is public domain. The whole period of the data lasts for 28 days from February 4 to March 3, 2013. By measuring the speed of vehicles in four lanes at a certain point on the highway 12 times at five-minute intervals, a 12×4 matrix is generated per hour. 24 such matrices are generated per day, so the dataset is a $24 \times 12 \times 4$ tensor. Further, since we use these tensors for 28 days, the size of the resulting tensor is $28 \times 24 \times 12 \times 4$. We artificially generated defects in this tensor. As practical situations, we assume that a disorder of a lane’s speedometer causes random and continuous deficiencies. We prepared three patterns of missing cases: a case with a disorder in the speedometer in lane 1 (scenario 1), a case with disorders in the speedometers in lanes 1, 2, and 3 (scenario 2), and a case with disorders in all speedometers (scenario 3). The missing rates for scenarios 1, 2, and 3 were 9%, 27%, and 34%, respectively. The source code for imparting deficits are available in the Supplementary Materials.

D.3 For comparison with non-negative tensor ring decomposition

Synthetic Datasets We create D core tensors with the size (R, I, R) by sampling from uniform distribution. Then a tensor with the size I^D and the tensor ring rank (R, \dots, R) is obtained by the product of these D tensors. Results for $R = 15, D = 5, I = 30$ are shown in the left column in Figure 4, and those for $R = 10, D = 6, I = 20$ in the right column in Figure 4. For all experiments on synthetic datasets, we change the target ring-rank as (r, \dots, r) for $r = 2, 3, \dots, 9$ for baseline methods.

Real Datasets TT_ChartRes is originally a $(736, 736, 31)$ tensor, which is produced from TokyoTech 31-band Hyperspectral Image Dataset. We downloaded ChartRes.mat from the official webpage³. We reshaped the tensor as $(23, 8, 4, 23, 8, 4, 31)$. For baseline methods, we chose the target ring-rank as $(2, 2, 2, 2, 2, 2, 2)$, $(2, 2, 2, 2, 2, 2, 5)$, $(2, 2, 2, 2, 2, 2, 8)$, $(3, 2, 2, 3, 2, 2, 5)$, $(2, 2, 2, 2, 2, 9)$, $(3, 2, 2, 3, 2, 2, 6)$, $(4, 2, 2, 2, 2, 2, 6)$, $(3, 2, 2, 4, 2, 2, 8)$, $(3, 2, 2, 3, 2, 2, 9)$, $(3, 2, 2, 3, 2, 2, 10)$, $(3, 2, 2, 3, 2, 2, 12)$, $(3, 2, 2, 3, 2, 2, 15)$, or $(3, 2, 2, 3, 2, 2, 16)$. TT_Origami is originally $(512, 512, 59)$ tensor, which is produced from TokyoTech 59-band Hyperspectral Image Dataset. We downloaded Origami.mat from the official webpage⁴. In TT_Origami, 0.0016% of elements were negative, hence we preprocessed all elements of TT_Origami by subtracting -0.000764 , the smallest value in TT_Origami, to make all elements non-negative. We reshaped the tensor as $(8, 8, 8, 8, 8, 59)$. For baseline methods, we chose the target ring-rank as $(2, 2, 2, 2, 2, r)$ for $r = 2, 3, \dots, 15$. These reshaping reduces the computational complexity as described in Section B.2 to complete the experiment in a reasonable time.

²<http://pems.dot.ca.gov/>

³<http://www.ok.sc.e.titech.ac.jp/res/MSI/MSIdata31.html>

⁴<http://www.ok.sc.e.titech.ac.jp/res/MSI/MSIdata59.html>

Algorithm 1: Many-body approximation

```

MANYBODYAPPROXIMATION( $\mathcal{T}, B$ )
   $s \leftarrow$  Total sum of  $\mathcal{T}$ .
  Obtain normalized input tensor  $\mathcal{P} \leftarrow \mathcal{T} ./ s$            // “./” denotes element-wise division
  Compute  $\hat{\eta}$  of  $\mathcal{P}$  using Equation (3).
  Initialize  $\theta_{t=1}^B$                                          // e.g.  $\theta_b = 0$  for all  $b \in B$ 
   $t \leftarrow 1$ 
  repeat
    Compute  $\mathcal{Q}_t$  using the current parameter  $\theta_t^B$  with Equation (1).
    Compute  $\eta_t^B$  from  $\mathcal{Q}_t$  using Equation (3).
    Compute the inverse of the Fisher information matrix  $\mathbf{G}$  using Equation (5).
     $\theta_{t+1}^B \leftarrow \theta_t^B - \mathbf{G}^{-1}(\eta_t^B - \hat{\eta}^B)$ 
     $t \leftarrow t + 1$ 
  until  $\|\eta_t^B - \hat{\eta}^B\| < \epsilon$                                 // We set  $\epsilon = 10^{-5}$  in our implementation;
   $\bar{\mathcal{T}} \leftarrow \mathcal{Q}_t .* s$                                 // “.*” denotes element-wise multiplication
  return  $\bar{\mathcal{T}}$ 

```

E Implementation detail

We describe the implementation details of methods in the following. All methods are implemented in Julia 1.8.

Environment Experiments were conducted on Ubuntu 20.04.1 with a single core of 2.1GHz Intel Xeon CPU Gold 5218 and 128GB of memory.

E.1 Proposed method

Many-body approximation We use a natural gradient method for many-body approximation. The natural gradient method uses the inverse of the Fisher information matrix to perform second-order optimization in a non-euclidean space. For non-normalized tensors, we conduct the following procedure. First, we compute the total sum of elements of an input tensor. Then, we normalize the tensor. After that, we conduct Legendre decomposition for the normalized tensor. Finally, we get the product of the result of the previous step and the total sum we compute initially. That procedure is justified by the general property of the KL divergence $\lambda D_{KL}(\mathcal{P}, \mathcal{Q}) = D_{KL}(\lambda \mathcal{P}, \lambda \mathcal{Q})$, for any $\lambda \in \mathbb{R}_{>0}$. The termination criterion is the same as the original implementation of Legendre decomposition by [39], that is, it terminates if $\|\eta_t^B - \hat{\eta}^B\| < 10^{-5}$, where η_t^B is the expectation parameters on t -th step and $\hat{\eta}^B$ is the expectation parameters of an input tensor, which are defined in Section 2.1.1. The overall procedure is described in Algorithm 1. Note that this algorithm is based on Legendre decomposition by [39].

LBTC The overall procedure is described in Algorithm 2 with our tolerance threshold. We randomly initialize each missing element in \mathcal{P}^1 by Gaussian distribution with mean 50 and variance 10.

E.2 Baselines

Baseline methods for tensor completion We implemented baseline methods for tensor completion by translating pseudo codes in original papers into Julia code. As baseline methods, we use HaLRTC, SiLRTC [21], SiLRTC-TT [3], and PTRCRW [42]. SiLRTC and HaLRTC are well-known classical methods based on HOSVD. SiLRTC-TT is based on tensor train decomposition. PTRCRW is based on tensor-ring decomposition and is known as state-of-the-art. HaLRTC requires a real value ρ and a weight vector α . We use the default setting on α described in the original paper and tune the value ρ as $\rho = 10^{-5}, 10^{-4}, \dots, 10^2$. SiLRTC requires a hyperparameter γ_d for $d = 1, 2, 3, 4$. This is the threshold of truncated SVD for the mode- d matrixization of the input tensor. Following the original paper, we assume $\gamma = \gamma_1 = \dots = \gamma_4$ and we tune γ in the range of $\{10^{-2}, 10^{-1}, \dots, 10^4\}$. SiLRTC-TT requires a weight vector α and a real number f . We set the

Algorithm 2: Low-body tensor completion

```

LBTC( $\mathcal{T}, B, \Omega$ )
   $t \leftarrow 1$ 
  Initialize  $\mathcal{P}^t$  // e.g. a random tensor
   $\mathcal{P}_\Omega^t \leftarrow \mathcal{T}_\Omega$ 
  repeat
     $\mathcal{P}^{t+1} \leftarrow \text{MANYBODYAPPROXIMATION } (\mathcal{P}^t, B)$  // m-step
     $\mathcal{P}_\Omega^{t+1} \leftarrow \mathcal{T}_\Omega$  // e-step
     $\text{res}^t \leftarrow \|\mathcal{P}^{t+1} - \mathcal{P}^t\|_F / \|\mathcal{P}^t\|_F$ 
     $t \leftarrow t + 1$ 
  until  $\text{res}^t - \text{res}^{t-1} < \epsilon$  and  $t > 2$  // We set  $\epsilon = 10^{-5}$  in our implementation;
  return  $\mathcal{P}$ 

```

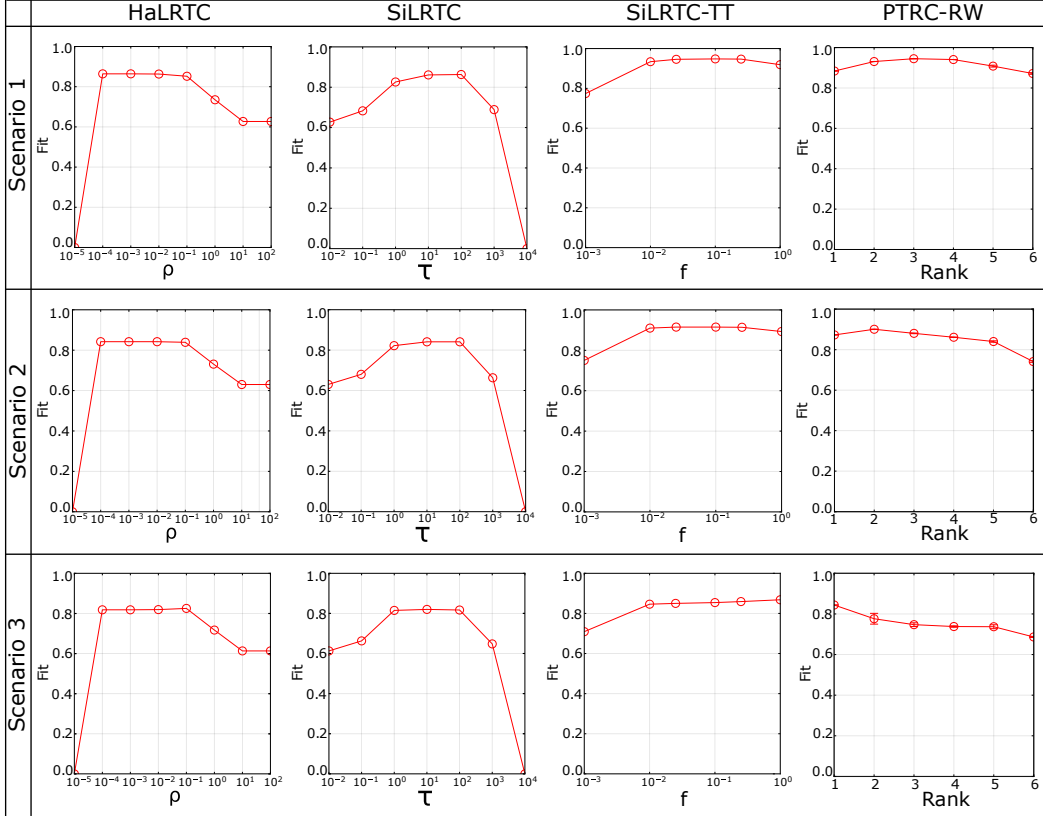


Figure 14: Hyper-parameter dependencies for the performance of baselines in the experiment in Section 3.2.

value of α as the default setting described in the original paper. We tune the value of f in the range of $\{0.001, 0.01, 0.025, 0.1, 0.25, 1\}$. PTRC-RW requires two weight vectors, α and β , step length d , and tensor ring rank as hyper parameters. Following the original paper, we use the default setting for α , β , and d . Then we tune tensor ring rank $(R, \bar{R}, \bar{R}, \bar{R})$ within the range $R \in \{1, 2, \dots, 6\}$, assuming that it has the same values in each element, which is also assumed in the original paper. Since PTRC-RW is not a convex method, we repeat it ten times for each R with randomly sampled initial values by Gaussian distribution with mean 50 and variance 10. We provide Figure 14, which shows the sensitivity of the tensor completion performance with respect to changes of the above hyper-parameters. All the above baseline methods include iterative procedures. These iterations were stopped when the relative error between the previous and the current iteration is less than 10^{-5} or when the iteration count exceeds 1500 iterations.

Baseline methods for tensor ring decomposition We implemented baseline methods for tensor ring decomposition by translating MATLAB code provided by the authors into Julia code for fair comparison. As we can see from their original papers, NTR-APG, NTR-HALS, NTR-MU, NTR-MM and NTR-lraMM have an inner and outer loop to find a local solution. We repeat the inner loop 100 times. We stop the outer loop when the difference between the relative error of the previous and the current iteration is less than 10^{-4} . NTR-MM and NTR-lraMM require a diagonal parameter matrix Ξ . We define $\Xi = \omega I$ where I is an identical matrix and $\omega = 0.1$. The NTR-lraMM method performs low-rank approximation to the matrix obtained by mode expansion of an input tensor. The target rank is set to be 20. This setting is the default setting in the provided code. The initial positions of baseline methods were sampled from uniform distribution on $(0, 1)$.

Baseline methods for low-rank approximation We implemented NNTF by translating the pseudo-code in the original paper [36] into Julia code. The algorithm requires NMF in each iteration. For that, we also implement the most standard method, multiplicative update rules, following the paper [19]. We use default values of hyper parameters of `sklearn` [33] for NMF. For NTD, we translate TensorLy implementation [16] to Julia code, whose cost function is the Frobenius norm between input and output.

References

- [1] Amari, S. (2016). *Information Geometry and Its Applications*. Springer.
- [2] Amari, S.-I. (1998). Natural gradient works efficiently in learning. *Neural computation*, 10(2):251–276.
- [3] Bengua, J. A., Phien, H. N., Tuan, H. D., and Do, M. N. (2017). Efficient tensor completion for color image and video recovery: Low-rank tensor train. *IEEE Transactions on Image Processing*, 26(5):2466–2479.
- [4] Bishop, C. M. and Nasrabadi, N. M. (2006). *Pattern recognition and machine learning*, volume 4. Springer.
- [5] Cheng, S., Wang, L., Xiang, T., and Zhang, P. (2019). Tree tensor networks for generative modeling. *Physical Review B*, 99(15):155131.
- [6] Cichocki, A., Lee, N., Oseledets, I., Phan, A.-H., Zhao, Q., Mandic, D. P., et al. (2016). Tensor networks for dimensionality reduction and large-scale optimization: Part 1 low-rank tensor decompositions. *Foundations and Trends® in Machine Learning*, 9(4-5):249–429.
- [7] Cichocki, A., Mandic, D., De Lathauwer, L., Zhou, G., Zhao, Q., Caiafa, C., and Phan, H. A. (2015). Tensor decompositions for signal processing applications: From two-way to multiway component analysis. *IEEE signal processing magazine*, 32(2):145–163.
- [8] Erol, A. and Hunyadi, B. (2022). Tensors for neuroimaging: A review on applications of tensors to unravel the mysteries of the brain. *Tensors for Data Processing*, pages 427–482.
- [9] Evenbly, G. and Vidal, G. (2015). Tensor network renormalization. *Physical review letters*, 115(18):180405.
- [10] Ghalamkari, K. and Sugiyama, M. (2021). Fast tucker rank reduction for non-negative tensors using mean-field approximation. In *Advances in Neural Information Processing Systems*, volume 34, pages 443–454, Virtual Event.
- [11] Ghalamkari, K. and Sugiyama, M. (2022). Fast rank-1 NMF for missing data with KL divergence. In *Proceedings of the 25th International Conference on Artificial Intelligence and Statistics*, pages 2927–2940, Virtual Event.
- [12] Ghalamkari, K. and Sugiyama, M. (2023). Non-negative low-rank approximations for multi-dimensional arrays on statistical manifold. *Information Geometry*.
- [13] Hitchcock, F. L. (1927). The expression of a tensor or a polyadic as a sum of products. *Journal of Mathematics and Physics*, 6(1-4):164–189.

[14] Kim, Y.-D. and Choi, S. (2007). Nonnegative tucker decomposition. In *2007 IEEE Conference on Computer Vision and Pattern Recognition*, pages 1–8. IEEE.

[15] Kolda, T. G. and Bader, B. W. (2009). Tensor decompositions and applications. *SIAM review*, 51(3):455–500.

[16] Kossaifi, J., Panagakis, Y., Anandkumar, A., and Pantic, M. (2019). Tensorly: Tensor learning in python. *Journal of Machine Learning Research*, 20(26):1–6.

[17] Kullback, S. and Leibler, R. A. (1951). On information and sufficiency. *The annals of mathematical statistics*, 22(1):79–86.

[18] LeCun, Y., Chopra, S., Hadsell, R., Ranzato, M., and Huang, F. (2006). A tutorial on energy-based learning. *Predicting structured data*, 1(0).

[19] Lee, D. and Seung, H. S. (2000). Algorithms for non-negative matrix factorization. *Advances in neural information processing systems*, 13.

[20] Levin, M. and Nave, C. P. (2007). Tensor renormalization group approach to two-dimensional classical lattice models. *Physical review letters*, 99(12):120601.

[21] Liu, J., Musialski, P., Wonka, P., and Ye, J. (2013). Tensor completion for estimating missing values in visual data. *IEEE Transactions on Pattern Analysis and Machine Intelligence*, 35(1):208–220.

[22] Luo, Y., Wang, F., and Szolovits, P. (2017). Tensor factorization toward precision medicine. *Briefings in bioinformatics*, 18(3):511–514.

[23] Malik, O. A. and Becker, S. (2021). A sampling-based method for tensor ring decomposition. In *International Conference on Machine Learning*, pages 7400–7411. PMLR.

[24] Monno, Y., Kiku, D., Tanaka, M., and Okutomi, M. (2017). Adaptive residual interpolation for color and multispectral image demosaicking. *Sensors*, 17(12):2787.

[25] Monno, Y., Kikuchi, S., Tanaka, M., and Okutomi, M. (2015). A practical one-shot multispectral imaging system using a single image sensor. *IEEE Transactions on Image Processing*, 24(10):3048–3059.

[26] Murg, V., Verstraete, F., Legeza, Ö., and Noack, R. M. (2010). Simulating strongly correlated quantum systems with tree tensor networks. *Physical Review B*, 82(20):205105.

[27] Murg, V., Verstraete, F., Schneider, R., Nagy, P. R., and Legeza, O. (2015). Tree tensor network state with variable tensor order: An efficient multireference method for strongly correlated systems. *Journal of Chemical Theory and Computation*, 11(3):1027–1036.

[28] Narita, A., Hayashi, K., Tomioka, R., and Kashima, H. (2012). Tensor factorization using auxiliary information. *Data Mining and Knowledge Discovery*, 25:298–324.

[29] Nayar and Murase, H. (1996). Columbia object image library: Coil-100. Technical Report CUCS-006-96, Department of Computer Science, Columbia University.

[30] Nielsen, M. A. and Chuang, I. L. (2010). *Quantum Computation and Quantum Information: 10th Anniversary Edition*. Cambridge University Press.

[31] Oseledets, I. V. (2011). Tensor-train decomposition. *SIAM Journal on Scientific Computing*, 33(5):2295–2317.

[32] Panagakis, Y., Kossaifi, J., Chrysos, G. G., Oldfield, J., Nicolaou, M. A., Anandkumar, A., and Zafeiriou, S. (2021). Tensor methods in computer vision and deep learning. *Proceedings of the IEEE*, 109(5):863–890.

[33] Pedregosa, F., Varoquaux, G., Gramfort, A., Michel, V., Thirion, B., Grisel, O., Blondel, M., Prettenhofer, P., Weiss, R., Dubourg, V., Vanderplas, J., Passos, A., Cournapeau, D., Brucher, M., Perrot, M., and Duchesnay, E. (2011). Scikit-learn: Machine learning in Python. *Journal of Machine Learning Research*, 12:2825–2830.

[34] Ran, B., Tan, H., Feng, J., Liu, Y., and Wang, W. (2015). Traffic speed data imputation method based on tensor completion. *Computational intelligence and neuroscience*, 2015:22–22.

[35] Shashua, A. and Hazan, T. (2005). Non-negative tensor factorization with applications to statistics and computer vision. In *Proceedings of the 22nd international conference on Machine learning*, pages 792–799.

[36] Shcherbakova, E. and Tyrtyshnikov, E. (2020). Nonnegative tensor train factorizations and some applications. In *Large-Scale Scientific Computing: 12th International Conference, LSSC 2019, Sozopol, Bulgaria, June 10–14, 2019, Revised Selected Papers 12*, pages 156–164. Springer.

[37] Shi, Y.-Y., Duan, L.-M., and Vidal, G. (2006). Classical simulation of quantum many-body systems with a tree tensor network. *Physical review a*, 74(2):022320.

[38] Sugiyama, M., Nakahara, H., and Tsuda, K. (2017). Tensor balancing on statistical manifold. In *Proceedings of the 34th International Conference on Machine Learning (ICML)*, volume 70 of *Proceedings of Machine Learning Research*, pages 3270–3279, Sydney, Australia.

[39] Sugiyama, M., Nakahara, H., and Tsuda, K. (2018). Legendre decomposition for tensors. In *Advances in Neural Information Processing Systems 31*, pages 8825–8835, Montréal, Canada.

[40] Tucker, L. R. (1966). Some mathematical notes on three-mode factor analysis. *Psychometrika*, 31(3):279–311.

[41] Walczak, B. and Massart, D. (2001). Dealing with missing data: Part i. *Chemometrics and Intelligent Laboratory Systems*, 58(1):15–27.

[42] Yu, J., Zhou, G., Li, C., Zhao, Q., and Xie, S. (2021a). Low tensor-ring rank completion by parallel matrix factorization. *IEEE Transactions on Neural Networks and Learning Systems*, 32(7):3020–3033.

[43] Yu, Y., Xie, K., Yu, J., Jiang, Q., and Xie, S. (2021b). Fast nonnegative tensor ring decomposition based on the modulus method and low-rank approximation. *Science China Technological Sciences*, 64(9):1843–1853.

[44] Yu, Y., Zhou, G., Zheng, N., Qiu, Y., Xie, S., and Zhao, Q. (2022). Graph-regularized non-negative tensor-ring decomposition for multiway representation learning. *IEEE Transactions on Cybernetics*.

[45] Zhang, S., Wang, W., Ford, J., and Makedon, F. (2006). Learning from incomplete ratings using non-negative matrix factorization. In *Proceedings of the 2006 SIAM international conference on data mining*, pages 549–553. SIAM.

[46] Zhao, Q., Zhou, G., Xie, S., Zhang, L., and Cichocki, A. (2016). Tensor ring decomposition. *arXiv preprint arXiv:1606.05535*.